Experimental and Numerical Investigations on Fracture Process Zone of Rock-Concrete Interface

Wei Dong[1,*], Dong Yang[2], Xiangming Zhou[3], Gediminas Kastiukas[4], Binsheng Zhang[5]

[1]Associate Professor, State Key Laboratory of Coastal and Offshore Engineering, Dalian University of Technology & Ocean Engineering Joint Research Center of DUT-UWA, Dalian 116024, P. R. China

*Corresponding author: E-mail: dongwei@dlut.edu.cn

[2]Postgratuate student, State Key Laboratory of Coastal and Offshore Engineering, Dalian University of Technology, Dalian 116024, P. R. China. E-mail: dongyang@mail.dlut.edu.cn

[3]Reader, Department of Mechanical, Aerospace and Civil Engineering, Brunel University London, Uxbridge, Middlesex UB8 3PH, United Kingdom & Haitian Visiting Professor, State Key Laboratory of Coastal and Offshore Engineering, Dalian University of Technology, Dalian 116024, P. R. China. E-mail: Xiangming.Zhou@brunel.ac.uk

[4]Ph.D student, Department of Mechanical, Aerospace and Civil Engineering, Brunel University, London, UB8 3PH, United Kingdom. Email: Gediminas.Kastiukas@brunel.ac.uk

[5]Senior Lecturer, Department of Construction and Surveying, School of Engineering and Built Environment, Glasgow Caledonian University, Glasgow G4 0BA, Scotland, United Kingdom. E-mail: Ben.Zhang@gcu.ac.uk

ABSTRACT

A crack propagation criterion for a rock-concrete interface is employed to investigate the evolution of the fracture process zone (FPZ) in rock-concrete composite beams under three-point bending (TPB). According to the criterion, cracking initiates along the interface when the difference between the mode I stress intensity factor (SIF) at the crack tip caused by external loading and the one caused by the cohesive stress acting on the fictitious crack surfaces reaches the initial fracture toughness of a rock-concrete interface. From the experimental results of the composite beams with various initial crack lengths but equal depths under TPB, the interface fracture parameters are determined. In addition, the FPZ evolution in a TPB specimen is investigated by using a digital image correlation (DIC) technique. Thus, the fracture processes of the rock-concrete composite beams can be simulated by introducing the initial fracture criterion to determine the crack propagation. By comparing the load versus crack mouth opening displacement (CMOD) curves and FPZ evolution, the numerical and experimental results show a reasonable agreement, which verifies the numerical method developed in this study for analysing the crack propagation along the rock-concrete interface. Finally, based on the numerical results, the effect of ligament length on the FPZ evolution and the variations of the fracture model during crack propagation are discussed for the rock-concrete interface fracture under TPB. The results indicate that ligament length significantly affects the FPZ evolution at the rock-concrete interface under TPB, and the stress intensity factor ratio of mode II to I is influenced by the specimen size during the propagation of the interfacial crack.

Keywords: Rock-concrete interface; Interfacial fracture; FPZ evolution; Crack

propagation; Numerical simulation.

Nomenclature

a	= crack length including cohesive crack length
A	= interfacial area
A_{lig}	= ligament area of the composite specimen
$CMOD$	= crack mouth opening displacement
D	= depth of specimen
DIC	= digital image correlation
E_{i}	= Young's modulus
f_{t}	= uniaxial tensile strength
f_{c}	= uniaxial compressive strength
FPZ	= fracture process zone
G_{f}	= fracture energy of concrete
$GMTS$	= Generalised maximum tangential stress criterion
$K_{\mathrm{I}}^{\mathrm{P}}$	= stress intensity factor of mode I caused by external loading
K_{I}^{σ}	= of mode I caused by cohesive stress
$K_{\mathrm{IC}}^{\mathrm{ini}}$	= initial stress intensity factor fracture toughness
$K_{\mathrm{IRC}}^{\mathrm{ini}}$	= initial fracture toughness of rock-concrete interface
K_{i}	= stress intensity factors
$L_{\mathrm{FPZ}}^{\max}$	= full FPZ length
l_{FPZ}	= FPZ length
$LEFM$	= linear elastic fracture mechanics
P_{ini}	= initial cracking load
$P_{\max}$	= peak load
P_{w}	= self-weight of the composite specimen

TPB = three-point bending

W_0 = area under the load-deformation curve

w = crack opening displacement

w_0 = stress-free crack opening displacement

w_s = crack opening displacement at the breaking point

$\triangle a$ = crack propagation length

δ_x = relative crack surface displacement in x direction

δ_y = relative crack surface displacement in y direction

δ_0 = deformation when load decreases to 0

σ = cohesive stress

σ_s = cohesive stress at the breaking point

INTRODUCTION

The bonded interface between dissimilar materials, such as the interface between a concrete gravity dam and the bedrock, is always a weak link, promoting crack initiation and leading to fracture even under service loads. The linear-elastic fracture mechanics (LEFM) developed by Rice[1] has been extensively accepted as a suitable technique to analyse and evaluate the potential fracture at a bi-material interface. Based on LEFM, some interfacial fracture parameters such as fracture energy and fracture toughness were investigated through experimental and numerical studies[2-4]. The experimental studies indicated that the magnitude of interfacial roughness would impact the aforementioned interfacial fracture parameters, driving researchers to study its effect by investigating specimens with smooth interfaces[5] and artificial grooving interfaces[6]. In addition, it was found that unlike homogeneous materials, the bonded interface between dissimilar materials, owing to the mismatching material properties, is always under the combination stress state of normal and shear stresses even under the conditions of symmetric geometries and balanced external loading. Through analyzing the interfacial fracture under various combinations of shear and normal stresses[7,8], it was found that the fracture of the specimen along the interface always corresponded to lower mixed mode stress intensity factor (SIF) ratios. On the contrary, the cracks for higher mixed mode stress intensity factor ratios usually diverted to one side of the interface[6,9]. In addition, the interfacial crack was inclined to kink into the weaker material when there exists a large difference in material properties between two sides of the interface[10]. In order to illustrate the fracture mechanism of an interface with respect to different failure modes, i.e. the crack propagates along the interface and diverts to one side of the interface, the nonlinear fracture theory, in which the strain localisation and nonlinear characteristics of the interface are taken into account, should be introduced to replace LEFM in the analysis of the interfacial fracture process.

For quasi-brittle materials, the fracture process zone (FPZ) lies in front of the crack tip, and attracts significant concerns when studying the nonlinear response of an engineering structure constructed with quasi-brittle materials during the fracture process. The effect of the FPZ on the fracture parameters of concrete, as a type of quasi-brittle material, has been extensively investigated in the last few decades. The size effect of the specific fracture energy was found to be related with the FPZ properties[11,12], demonstrating that the FPZ length in particular decreases rapidly when the crack propagates close to the top surface of a specimen. Consequently, the local fracture energy was found to be not constant during the whole fracture process, and instead decreased with the reduction of the FPZ length.

Combining the theoretical and experimental studies, a bilinear model on local fracture energy distribution was proposed to calculate the true specific fracture energy[13]. The significant effect of a varying FPZ on concrete fracture characteristics and the entire fracture process has engaged scientific and engineering communities. The relevant studies have been carried out through experimental investigations[14-16] and numerical simulations[17,18]. In addition, as one three-dimensional effect on fracture analysis, a coupled fracture mode was found to exist in cracked thick plate under shear or out-plane loading, and the intensity of the coupled mode was significantly influenced by the thickness of plate in three-dimensional finite element (FE) analysis[19-21]. However, the study on the evolution of the FPZ during the complete fracture process at a rock-concrete interface has been little reported. Regarding the rock-concrete interfacial fracture, it is worthwhile to point out that the derived fracture energy based on LEFM without considering the FPZ is less than that based on nonlinear fracture mechanics[22] by 83% . Therefore, it is significant to incorporate the study of the FPZ evolution at the rock-concrete interface when exploring the fracture mechanism and assessing the nonlinear response of a concrete structure constructed on bedrock.

Meanwhile, the crack propagation criteria in numerical methods have been widely investigated, which demonstrate the mechanism of crack growth in quasi-brittle materials like concrete. The criterion based on the maximum principle tensile stress has been adopted to simulate fracture processes of concrete by many researchers[22-24]. In this criterion, the accuracy of the calculated stress at a crack tip is largely influenced by element meshing and computational method. Therefore, to avoid getting misleading stress values at the crack tip, the stress intensity factor (SIF) - based criteria have been employed in the analyses of fracture processes, and gained increasing attentions in the research communities. One type of SIF-based criteria was proposed by Carpinteri and Massabó[25], in which the crack begins to propagate when the stress singularity at the tip of the cohesive zone vanishes, i.e. SIF is equal to 0. Later, this propagation criterion was also applied to study the crack growth in concrete[26], other quasi-brittle materials[27] and composite materials with a rock-concrete interface[6]. The other SIF-based criteria proposed by Dong[28] for determining the crack propagation in concrete states that a crack initiates when the difference in the SIFs at the crack tip caused by external loading and the cohesive stress reaches the initial fracture toughness of concrete. The comparison of the two SIF-based criteria in the analysis of crack propagation in concrete has been made, and the applicability of the criteria has been discussed for concrete at various strength levels[29]. The concept of the SIF-based criterion by Dong[28] was also coupled with the maximum circumferential stress criterion to investigate mixed mode I-II fracture in concrete[30]. In addition, a generalized maximum tangential stress criterion (GMTS) considering T-stress was also employed to analyze the fracture of granite under four-point bend loading[31]. However all studies mentioned above do not pertain to specimens with blunt notches or U-notches. Considering the complex stress distribution at the notch tip under mixed mode loading, a strain energy density (SED)-based[32] and crack zone model (CZM)-based[33] fracture criterion were used to predict the critical load for blunt U- and V-notched brittle specimens[34-36]. Meanwhile, together with the crack propagation or fracture criteria, numerical methods such as the finite element method[28,37], extended finite element method[26] and scaled boundary finite element method[6] have been employed to simulate crack growth. These numerical methods provide an additional, effective tool to study the FPZ evolution in both quasi-brittle materials and interfacial zones. Particularly, it is more convenient to employ numerical methods to study the size effect of the FPZ evolution which cannot be easily achieved through experimental investigations.

Therefore, the main objective of this paper is to employ a stress intensity factor (SIF) -based crack propagation criterion to investigate the FPZ evolution during the complete fracture process along a rock-concrete interface. Firstly, rock-concrete composite beams with different initial crack ratios are tested under TPB. Moreover, a DIC technique is used to investigate the FPZ evolution at the rock-concrete interface. The load versus crack mouth opening displacement (P-CMOD) curves (measured using one clip gauge mounted on the bottom surface of the specimen), crack surface opening displacement (measured through the digital image correlation technique) and the FPZ evolution based on the experimental results are compared with those from the numerical approach to verify the numerical method established in this study. Finally, the FPZ properties of composite beams with a rock-concrete interface are discussed based on the experimental and numerical results. It is expected that the experimental and numerical results presented here can lead to a better understanding of the FPZ evolution of a rock-concrete interfaces so that nonlinear fracture mechanics can be more efficiently employed to the analysis on crack propagation.

NUMERICAL METHOD

The crack propagation criterion which implements the initial fracture toughness has been adopted to successfully simulate the crack growth of mode I and mixed mode fracture in concrete[17,28,30]. This criterion for mode I crack propagation can be described by the following formula:

$$K_I^P + K_I^\sigma = K_{IC}^{ini} \tag{1}$$

where K_I^P and K_I^σ are the mode I SIFs caused by external loading and cohesive stress, respectively, and K_{IC}^{ini} is the initial fracture toughness of concrete. In order to calculate K_I^σ, the softening traction-separation law, i.e. the tension-softening relationship, should be adopted to determine the distribution of cohesive stress on a crack surface. Meanwhile, K_{IC}^{ini} can be regarded as a material property, which represents the capability of concrete to resist crack-initiation[38,39]. Based on the criterion, the whole fracture process of a beam under particular TPB can be described as a collection of critical crack-initiation states for a series of geometrically similar beams but with different effective crack lengths[28].

In the case of a rock-concrete interface, however, the crack propagation criterion mentioned above cannot be directly applied to investigate the crack growth at a rock-concrete interface. Calculating the SIFs at the crack tip for a bi-material interface is different from that for a homogeneous material. To make a distinction, the SIFs for a bi-material interface are always denoted as K_1 and K_2 instead of K_I and K_{II} in this paper. Generally, they are calculated through numerical methods, e.g. stress or displacement extrapolations. In this paper, the SIFs for a rock-concrete interface crack are calculated by the displacement extrapolation method using the ANSYS finite element code with the formulas shown as follows[40]:

$$K_1 = C \lim_{r\to 0}\sqrt{\frac{2\pi}{r}}\left[\delta_y(\cos Q + 2\varepsilon \sin Q) + \delta_x(\sin Q - 2\varepsilon \cos Q)\right] \tag{2}$$

$$K_2 = C \lim_{r\to 0}\sqrt{\frac{2\pi}{r}}\left[\delta_y(\cos Q + 2\varepsilon \sin Q) - \delta_x(\sin Q - 2\varepsilon \cos Q)\right] \tag{3}$$

where

$$C = \frac{2\cosh(\varepsilon\pi)}{(\kappa_1+1)/\mu_1+(\kappa_2+1)/\mu_2} \tag{4}$$

$$Q = \varepsilon \ln r \tag{5}$$

$$\varepsilon = \frac{1}{2\pi}\ln\left(\frac{\frac{\kappa_1}{\mu_1}+\frac{1}{\mu_2}}{\frac{\kappa_2}{\mu_2}+\frac{1}{\mu_1}}\right) \tag{6}$$

$$\mu_i = \frac{E_i}{2(1+v_i)} \qquad (i=1,2) \tag{7}$$

$$\kappa_i = \begin{cases}(3-v_i)/(1+v_i) & (Plain\ stress)\\(3-4v_i) & (Plain\ strain)\end{cases} \tag{8}$$

E_i, v_i, δ_x and δ_y are the Young's modulus, Poisson's ratio, and the relative crack surface displacements in x and y directions, respectively.

As previously mentioned, crack growth along a rock-concrete interface is in fact a mixed mode fracture process. However, it should be noted that K_2 is far less than K_1 for a TPB beam[4]. As a consequence, the crack propagation along the rock-concrete interface in a TPB beam can be approximately considered as a mode I-dominated fracture process. Moreover, a bilinear relationship between cohesive stress (σ) and crack opening displacement (w) for a rock-concrete interface[41] is adopted in the numerical method, which is shown in Fig. 1. The crack opening displacement w_s and the corresponding cohesive stress σ_s at the breaking-point of the bilinear σ-w relationship is equal to $0.8G_f/f_t$ and $0.2f_t$, respectively. The stress-free crack opening displacement w_0 equals to $6G_f/f_t$. Here, f_t and G_f are the uniaxial tensile strength and fracture energy of a rock-concrete interface, respectively. A direct tension test was conducted to measure the uniaxial tensile strength of the rock-concrete interface. 100 mm × 100 mm × 200 mm prisms were prepared, which consisted of two geometrically identical blocks, i.e. rock and concrete block, respectively. The uniaxial tensile strength, f_t, is calculated from the following equation:

$$f_t = P_{max}/A \tag{9}$$

where P_{max} is the peak load, and A is the interfacial area.

In this paper, the crack propagation criterion is modified and extended to determine the crack growth along the rock-concrete interface of a composite beam under TPB. The modified crack propagation criterion for a rock-concrete interface can be expressed as following:

$$K_1^P + K_1^{\sigma} = K_{1RC}^{ini} \tag{10}$$

In Eq. (10), K_1^P and K_1^{σ} can be calculated by inserting the relative crack surface displacements δ_x and δ_y to Eqs. (2) and (3). Thus, the initial fracture toughness of the rock-concrete interface, K_{1RC}^{ini} can be calculated by deriving δ_x and δ_y with respect to the initial cracking load P_{ini}. Using the crack propagation criterion, the corresponding load at any certain crack length can be derived. Thus, the complete crack propagation process can be simulated, in which the details of the iterative process can be referred to elsewhere[28].

EXPERIMENTAL PROGRAM

To verify the proposed crack propagation criterion, a series of composite beams with a rock-concrete interface were tested under TPB to investigate the fracture process. The P-CMOD curves were derived from the experimental studies. In addition, taking a composite beam as an example, the FPZ evolution during the complete fracture process was also studied using a DIC technique.

Experimental specimens

The geometry of the rock-concrete composite beams and the test setup are illustrated in Fig 2(a). The dimensions of the composite beams are 500 mm × 100 mm × 100 mm. Each composite beam consists of two halves, a half concrete block and a half limestone block. It should be noted that to make a composite beam, concrete was cast against the half rock block with a natural surface which was obtained after a TPB test on a pre-notched rock beam (See Fig 2(b)). The rock beams have the same dimensions as the composite ones, but with different initial crack lengths. Five series of composite beams with a_0/D from 0.2 to 0.6, denoted as TPB20 to TPB60, were prepared, and three parallel composite beams were produced for each series. Grade 42.5R Portland cement, crushed stone with the maximum size of 10 mm and medium-size river sand were used for making concrete with a mix of 1:0.62:1.81:4.20 by weight (cement : water : sand : aggregate). The composite specimens were demolded one day after casting and then cured in an environment of 23℃ and 90% RH for 28 days. The material properties of rock, concrete and the interface were measured with the results presented in Table 1, in which E, v, f_c and f_t denote the elastic modulus, Poisson's ratio, compressive strength and uniaxial tensile strength, respectively.

Three-point bending tests

The three-point bending tests on the rock-concrete composite beams were performed using a 250kN closed-loop servo-hydraulic testing machine (MTS) under a displacement control loading mode at a rate of 0.012 mm/min. Both the displacement at the loading point and the CMOD were measured using clip gauges. In order to measure P_{ini}, four strain gauges were symmetrically attached at the pre-notch tip on both sides of a composite beam. Strain gauges and clip gauges, together with a load cell were connected to an Integrated

Measurement & Control (IMC) dynamic date acquisition device. The setup for the TPB testing is illustrated in Fig 3.

The fracture parameters of a composite beam with a rock-concrete interface including K_{1RC}^{ini}, P-CMOD curve and G_f were derived from the results of the three-point bending tests. Based on LEFM, in order to calculate the initial fracture toughness, P_{ini} should be determined. When a crack initiates and starts to propagate, the measured strain on the two sides of the crack will suddenly and significantly decrease due to the release of fracture energy. Therefore, P_{ini} can be determined according to the variation of the measured strain at the tip of a pre-crack. Meanwhile, G_f of the rock-concrete interface was derived from the load-deformation curves, which is the same procedure to concrete suggested by RILEM[42]. The deformation at the loading point can be measured using the clip gauge mounted on the top of the specimen (See Fig. 3). G_f can be calculated from the following equation:

$$G_f = \frac{W_0 + 2P_w\delta_0}{A_{lig}} \tag{11}$$

where W_0 is the area of load-deformation curves, P_w is the self-weight of the composite specimen, δ_0 is the deformation when the load decreases to 0, and A_{lig} is the ligament area of the composite specimen.

Digital image correlation (DIC) test

In order to verify the proposed crack propagation criterion and investigate the FPZ evolution along a rock-concrete interface during the entire fracture process, the displacement on the cracking surface of beam TPB30-1 was studied using a DIC technique, with the test setup shown in Fig. 4. Before performing the TPB test, white and black spray paint was used to create a speckle pattern on one side of the potential cracking surface of a

TPB30-1 beam. A digital camera with a resolution of 1024×768 pixels and a host-computer were used in the DIC test to measure the displacement on the crack surface. Images of the deformation were snapped by the digital camera every half a second and stored in a host-computer. The deformation field near the crack tip can be composed by comparing images of the crack surface before and during the loading. Therefore, the complete crack propagation process can be tracked using the opening and sliding displacements at the rock-concrete interface obtained directly by using the DIC imaging.

The computational domain is selected based on the potential crack propagation route, in which one analysis point was picked from every five pixels in both u and v directions (see Fig. 5). For beam TPB30-1, a total of 26128 (142×184) points were picked in the computational domain. The analysis lines M_iN_i (i = 1, 2, …, 184) were set for every five pixels apart in the v direction, in which the u and v displacements of each analysis point can be determined. In the numerical procedure, the u and v displacements of the analysis points located on M_1N_1 to M_iN_i lines were determined at each load level. According to the tension-softening constitutive law of a rock-concrete interface proposed by Dong[43], the critical crack opening displacement w_0 for beam TPB30-1 equals 0.0844 mm. Thus, the FPZ length and opening/sliding displacements can be determined at each load level. In addition, the trajectory of crack growth can be observed through the strain-contour diagram in the computational domain.

EXPERIMENTAL RESULTS AND NUMERICAL VERIFICATIONS

P-CMOD curves

It was observed from the experiment that the fracture of all composite beams was caused by crack propagation along their rock-concrete interface under TPB. The experimental results, which are listed in Table 2, show that initial fracture toughness of mode II, K_{2RC}^{ini}, is much less than that of mode I, K_{1RC}^{ini}. In order to verify the proposed propagation criterion, comparisons of the experimental and numerical P-CMOD curves are made, and the results are shown in Fig. 6. Moreover, relative material properties used in numerical simulation are listed in Table 3. It can be seen that the numerical results are in a reasonably good agreement with the experimental ones, indicating the validity of the proposed crack propagation criterion in the analysis of interfacial crack propagation.

FPZ evolution

In this paper, the crack propagation process of beam TPB30-1 was studied using the DIC technique. By considering the two loading stages, i.e., $P_1 = P_{max}$ and $P_2 = 11\%P_{max}$ at the post-peak branch, i.e. the strain-softening branch, as examples, the FPZ evolution and corresponding opening/sliding displacements are illustrated in Fig. 7. Moreover, the strain fields at the two loading stages are illustrated in Fig. 8. It can be seen from Fig. 7 that the crack sliding displacement is very small compared with the crack opening displacement, which indicates that the rock-concrete interface fracture under TPB is predominantly dominated by mode I fracture.

The FPZ evolution of beam TPB30-1 is also simulated using the numerical method based on the proposed crack propagation criterion. A comparison of the crack opening displacement field is made with respect to the loading levels P_1 and P_2 between the DIC and numerical results, which are shown in Figs. 9(a) and (b). Moreover, the FPZ evolution in the complete fracture process is also analyzed, and comparisons between numerical and experimental results are then made (see Fig. 10). It can be seen from Figs. 9 and 10 that the numerical results are in a reasonably good agreement with the experimental ones, which verifies the proposed numerical method in the analysis of FPZ evolution at a rock-concrete interface.

DISCUSSIONS ON FPZ EVOLUTION

The experimental results obtained under the current laboratory conditions in this study may to certain degree affect the expansion of the conclusions to practical engineering structures due to the size effect. From the viewpoint of structure reliability assessment, it is expected to have a better understanding of the size effect of FPZ evolution in quasi-brittle materials and along interfaces, so that the fracture mechanism of practical structures can be revealed reasonably and the failure process can be predicted precisely. In this section, the verified numerical method is used to investigate the FPZ evolution at a rock-concrete interface. Also the material properties used in the following numerical analyses are listed in Table 3.

Size effect on FPZ evolution

In order to investigate the effect of a_0/D on the FPZ evolution, the fracture process of the T series rock-concrete composite beams with the same size but different notch/depth (a_0/D) ratios is studied using numerical analysis. The geometries of the T series composite beams and the numerical results, including the initial cracking load P_{ini}, peak load $P_{\max}$ and full FPZ length $L_{FPZ}^{\max}$, are listed in Table 4. Fig. 11 shows the FPZ evolutions for the five T-series composite beams. It can be seen that the FPZ length, l_{FPZ}, linearly increases until the full FPZ length $L_{\mathrm{FPZ}}^{\max}$ is reached, and then decreases rapidly for all beams. With the increase of

a_0/D, i.e. the decrease of ligament length, the maximum FPZ length that can be attained decreases but the corresponding ratio of $\triangle a/(D - a_0)$ increases.

In addition, the effect of specimen size on the FPZ evolution is also studied on the L series composite beams with the same a_0/D but varied sizes (see Table 5). It should be noted that the whole fracture process of beams with a high depth cannot be obtained due to large self-weights of the specimens. Therefore the self-weight of the L series composite beams are disregarded in the numerical analyses. The FPZ evolutions of the L series beams are illustrated in Fig. 12. It can be seen that the ratio of L_{FPZ}^{max} to the ligament length ($D - a_0$) also gradually decreases as the depth D increases from 100 mm to 20000 mm (20 m). The FPZ length begins to decrease after the FPZ fully develops in cases of small specimens, e.g. Specimens L100 and L150. However, the declining tendency becomes slow with the increase of specimen size. Particularly, in the cases of D = 10 m and 20 m, the variations of the FPZ length are approximately steady as crack propagates after reaching the full FPZ. The results indicate that the FPZ evolution at a rock-concrete interface is largely dependent on the specimen size. Therefore, for concrete structures constructed on rock with a large ligament length, the FPZ will move forward with an almost constant length, i.e. the full FPZ length, under mode I-dominated fracture.

In order to explore the mechanism of FPZ evolution, the FPZ evolutions in the T and L series specimens are illustrated together in Fig. 13, which are arranged according to the ligament lengths. It can be observed that the ratio of L_{FPZ}^{max} to ($D - a_0$) decreases as the ligament length ($D - a_0$) increases. To further verify the specimen size effect on the FPZ evolution at a rock-concrete interface, the S series composite beams, which have the same ligament length but different a_0/D ratios, are also analysed in the study. The geometries of the S series beams and numerical results are presented in Table 6. The FPZ evolutions of the S series beams are illustrated in Fig. 14. It can be seen that the FPZ length remains equal for all the S series beams even though they have different a_0/D ratios. Therefore, based on the analyses of FPZ evolution in the L, T and S series beams, it can be concluded that the ligament length indeed affects the interfacial FPZ evolution and results in the size effect of FPZ. Meanwhile, it is also found that the ratio of $L_{\mathrm{FPZ}}^{\max}$ to $(D - a_0)$ decreases with the increase of the ligament length $(D - a_0)$, which indicates that LEFM is appropriate for fracture analysis of structures with larger ligament length for the purpose of simplified calculation.

Effect of specimen size on K_2/K_1 ratio

Under TPB, due to the materials being different on both sides of a crack, the rock-concrete interface is under mixed mode fracture rather than under single mode fracture. Therefore, the ratio of K_2/K_1 would vary as the crack propagates along the interface. For the T series specimens, K_2/K_1 versus a/D relationships are illustrated in Fig. 15. It can be seen that these curves almost coincide with each other although they have different starting points, i.e. different a_0/D ratios. Thus, in the case of specimens with the same size, the K_2/K_1 versus a/D curve with respect to the smallest a_0/D can be regarded as the envelope of those curves for the specimens with larger a_0/D ratios. The maximum value of K_2/K_1 is 0.172, which corresponds to a/D = 0.62.

In addition to the effect of a_0/D, the effect of specimen size on the K_2/K_1 ratio is also studied. Fig. 16(a) illustrates the variations of K_2/K_1 for Specimens L100, L150, L200 and

L250, and indicates that the value of K_2/K_1 increases with the increase of specimen size. However, it should be noted that, comparing with the initial K_2/K_1 corresponding to the initial crack length a_0, the increase is not significant for the maximum value of K_2/K_1. Taking Specimen L100 as an example, the initial K_2/K_1 is 0.15 and the maximum is 0.175. Therefore, the initial K_2/K_1 without crack propagation can approximately reflect the maximum ratio for mixed mode during the fracture process although the mode varies as the crack propagates. Moreover, the value of K_2/K_1 decreases rapidly when the crack is close to the top surface of a rock-concrete composite beam, leading the rock-concrete interface fracture to be mode I dominated at that moment.

On the other hand, the effect of a_0/D on the K_2/K_1 ratio also attracts attention of researchers who would measure the fracture parameters at rock-concrete interface under mode I fracture. Upon this point, the LEFM analysis is conducted to investigate the effect of a_0/D on the initial K_2/K_1 ratio in the initial cracking state since no crack propagation happens yet. In the analysis, the external load is set as a constant value, and the initial crack length is increased step by step. At each step, the corresponding K_2/K_1 at the crack tip is calculated. Taking Specimen T20 as an example, the variations of K_2/K_1 during the complete fracture process without considering the action of the cohesive stress are shown as the curve for T20L in Fig. 15. In fact, the curve presents the variations of the initial K_2/K_1 for the rock-concrete composite beams with the same size as T20 but varying a_0/D from 0.2 to 1.0. It can be seen from the curve that the value of K_2/K_1 increases slowly from a_0/D = 0.2 until the peak is reached, and then reduces. The ratio of K_2/K_1 reaches the peak value of 0.12 at point A when a/D is about 0.56. Fig. 16(b) illustrates the variations of K_2/K_1 with respect to

Specimens L100, L150, L200 and L250, without considering the effect of the cohesive force. Similar to the curve for T20L in Fig. 15, these curves also represent the variations of the initial K_2/K_1 for the specimens with the same size as L100, L150, L200 and L250 but varying a_0/D from 0.2 to 1.0. Based on the results in Fig. 16(b), it can be concluded that the initial K_2/K_1 is largely affected by the specimen size. With the increase of specimen size, the initial K_2/K_1 increases for the same a_0/D. Meanwhile, the value of K_2/K_1 decreases rapidly when the crack is close to the top surface of the specimen, which shows a similar tendency to the variations of K_2/K_1 considering the effect of FPZ. Although the pure mode I fracture can be approximately obtained for a TPB composite beam when a/D is close to 1, it is not convenient to conduct experiment in the lab because the large pre-crack length makes a specimen break easily. Therefore, it is more reasonable to test the specimens with small a_0/D and small geometry size to obtain the mode I fracture at a rock-concrete interface.

The peak values of K_2/K_1 for different specimens with/without considering the effect of FPZ are presented in Table 7. It can be seen from the table that the maximum values of K_2/K_1 of all specimens are reached when a/D is around 0.57. The difference between maximum K_2/K_1 value calculated with and without considering the effect of FPZ increases as the beam depth increases. This can be explained by the fact that higher beams have lager FPZ length so that the restriction of the cohesive stress on K_1 is more significant.

In order to further verify the effect of specimen size on the initial K_2/K_1, the analyses, based on LEFM, are conducted on various sizes of TPB specimens with a_0/D = 0.3. Fig. 17 illustrates the initial K_2/K_1 versus specimen depth D relationship. It can be seen from this figure that the value of K_2/K_1 increases as the specimen depth increases, and the relationship can be approximately expressed by using a logarithmic function. Curve fitting is hence applied and the corresponding logarithmic function can be obtained as follows:

$$K_2/K_1 = 0.1 \log(D) - 0.09 \tag{12}$$

According to the results shown in Fig. 17, in the case of rock-concrete interfacial fracture, the value of K_2/K_1 is close to 0.3 for large size specimens under TPB. Combining the results in Fig. 16 indicates that the ratio of K_2/K_1 would further increase during crack propagation due to the effect of FPZ. As a consequence, in the case of a concrete dam with a crack along the interface between the concrete dam and the rock foundation, the crack may divert into the rock foundation after propagating certain length due to the increase of K_2/K_1 during the fracture process.

CONCLUSIONS

A crack propagation criterion for a rock-concrete interface is proposed to investigate the FPZ evolution in rock-concrete composite beams under TPB. The experiments including the TPB testing and the DIC technique are conducted to measure the P-CMOD curves and the FPZ evolution. These results then are compared with the numerical simulations to verify the proposed criterion. Moreover, the numerical method combining with the proposed criterion is employed to study the effect of the ligament length on the FPZ evolution and the variations of fracture model during crack propagation for the rock-concrete interface fracture. The following conclusions can be drawn:

(a) By comparing with the P-CMOD curves and the FPZ evolutions from the experimental investigations, the numerical results show a reasonably good agreement, which verifies the proposed criterion in the analysis of rock-concrete interfacial fracture. Therefore, if the elastic moduli E of concrete and rock, the interfacial uniaxial tensile strength f_t, the interfacial fracture energy G_f and the initial fracture toughness K_{1RC}^{ini} are given, the complete fracture process at rock-concrete interface under TPB can be predicted based on the proposed numerical model.

(b) The ligament length significantly affects the FPZ evolution at a rock-concrete interface under TPB. Both experimental and numerical results show that the FPZ length linearly increases as crack propagates until the maximum FPZ length is reached, and decreases thereafter. In the case of a large ligament length, with the maximum of 14 m in this study, the decreasing tendency of the FPZ is slow and keeps an approximately plateau after its full development.

(c) The ratio of K_2/K_1 varies during the interfacial crack propagation under TPB, slowly increasing first and then decreasing. For specimens with different sizes, the maximum of K_2/K_1 can be achieved when a/D is approximate 0.57. When the crack is close the top surface of the specimen, the ratio of K_2/K_1 sharply decreases to 0, which indicates the fracture of the composite specimen is dominated by mode I failure. Specimen size affects the variations of K_2/K_1 during interfacial crack propagation. Larger K_2/K_1 ratios can be obtained for higher specimens under the same a/D. The initial K_2/K_1 ratio versus specimen depth relationship can be expressed using a logarithmic function.

ACKNOWLEDGEMENTS

The financial support of the National Natural Science Foundation of China under the grants of NSFC 51478083, NSFC 51421064 and NSFC 51109026, and the National Basic Research Program of China (973 Program, Grant No. 2015CB057703) is gratefully acknowledged.

REFERENCES

1. Rice, J. (1988) Elastic fracture mechanics concepts for interfacial cracks. *J. Appl. Mech.* **55**: 98-103.

2. Bank-Sills, L., N. Travitzky, D. Ashkenazi and R. Eliasi (1999) A methodology for measuring interface fracture properties of composite materials. *Int. J. Fracture*. **99**: 143-161.

3. Charalambides, P., J. Lund, A. Evans and R. McMeeking (1989) A test specimen for determining the fracture resistance of bimaterial interfaces. *J. Appl. Mech.* **56**: 77-82.

4. Kishen, J. C. and V. E. Saouma (2004) Fracture of rock-concrete interfaces: laboratory tests and applications. *ACI Struct. J.* **101**: 325-331.

5. Tian, H., W. Chen, D. Yang and J. Yang (2015) Experimental and numerical analysis of the shear behaviour of cemented concrete-rock joints. *Rock Mech. Rock Eng.* **48**: 213-222.

6. Zhong, H., E. T. Ooi, C. Song, T. Ding, G. Lin and H. Li (2014) Experimental and numerical study of the dependency of interface fracture in concrete-rock specimens on mode mixity. *Eng. Fract. Mech.* **124**: 287-309.

7. Tippur, H. V. and S. Ramaswamy (1993) Measurement of mixed-mode fracture parameters near cracks in homogeneous and bimaterial beams. *Int. J. Fracture*. **61**: 247-265.

8. Yang, S., L. Song, Z. Li and S. Huang (2008) Experimental investigation on fracture toughness of interface crack for rock/concrete. *Int. J. Mod. Phys. B*. **22**: 6141-6148.

9. Slowik, V., J. C. Kishen and V. E. Saouma (1998) Mixed mode fracture of cementitious bimaterial interfaces: Part I Experimental results. *Eng. Fract. Mech.* **60**: 83-94.

10. Porto, C., M. Parente, R. Jorge, L. Pereira and S. Griza (2016) Fracture toughness of the interface between Ni-Cr/ceramic, alumina/ceramic and zirconia/ceramic systems. *Fatigue Fract. Eng. M.* **39**: 817-829.

11. Hu, X. and K. Duan (2004) Influence of fracture process zone height on fracture energy of concrete. *Cement Concrete Res.* **34**: 1321-1330.

12. Hu, X. and F. Wittmann (2000) Size effect on toughness induced by crack close to free surface. *Eng. Fract. Mech.* **65**: 209-221.

13. Duan, K., X. Hu and F. Wittmann (2003) Boundary effect on concrete fracture and non-constant fracture energy distribution. *Eng. Fract. Mech.* **70**: 2257-2268.

14. Otsuka, K. and H. Date (2000) Fracture process zone in concrete tension specimen. *Eng. Fract. Mech.* **65**: 111-131.

15. Wu, Z., H. Rong, J. Zheng, F. Xu and W. Dong (2011) An experimental investigation on the FPZ properties in concrete using digital image correlation technique. *Eng. Fract. Mech.* **78**: 2978-2990.

16. Zhang, D. and K. Wu (1999) Fracture process zone of notched three-point-bending concrete beams. *Cement Concrete Res.* **29**: 1887-1892.

17. Dong, W., X. Zhou and Z. Wu (2013) On fracture process zone and crack extension resistance of concrete based on initial fracture toughness. *Constr. Build. Mater.* **49**: 352-363.

18. Liang, R. and Y.-N. Li (1991) Simulations of nonlinear fracture process zone in cementitious material — a boundary element approach. *Comput. Mech.* **7**: 413-427.

19. Kotousov, A., F. Berto, P. Lazzarin and F. Pegorin (2012) Three dimensional finite element mixed fracture mode under anti-plane loading of a crack. *Theor. Appl. Fract. Mec.*

62: 26-33.

20. Kotousov, A., P. Lazzarin, F. Berto and L. Pook (2013) Three-dimensional stress states at crack tip induced by shear and anti-plane loading. *Eng. Fract. Mech.* **108**: 65-74.

21. Pook, L. P., A. Campagnolo, F. Berto and P. Lazzarin (2015) Coupled fracture mode of a cracked plate under anti-plane loading. *Eng. Fract. Mech.* **134**: 391-403.

22. Červenka, J., J. C. Kishen and V. E. Saouma (1998) Mixed mode fracture of cementitious bimaterial interfaces: Part II numerical simulation. *Eng. Fract. Mech.* **60**: 95-107.

23. Gerstle, W. H. and M. Xie (1992) FEM modeling of fictitious crack propagation in concrete. *J. Eng. Mech.* **118**: 416-434.

24. Hillerborg, A., M. Modéer and P.-E. Petersson (1976) Analysis of crack formation and crack growth in concrete by means of fracture mechanics and finite elements. *Cement Concrete Res.* **6**: 773-781.

25. Carpinteri, A. and R. Massabó (1997) Reversal in failure scaling transition of fibrous composites. *J. Eng. Mech.* **123**: 107-114.

26. Moës, N. and T. Belytschko (2002) Extended finite element method for cohesive crack growth. *Eng. Fract. Mech.* **69**: 813-833.

27. Yang, Z. and A. Deeks (2007) Fully-automatic modelling of cohesive crack growth using a finite element–scaled boundary finite element coupled method. *Eng. Fract. Mech.* **74**: 2547-2573.

28. Dong, W., Z. Wu and X. Zhou (2013) Calculating crack extension resistance of concrete based on a new crack propagation criterion. *Constr. Build. Mater.* **38**: 879-889.

29. Dong, W., Z. Wu, X. Zhou and C. Wang (2016) A comparative study on two stress intensity factor-based criteria for prediction of mode-I crack propagation in concrete. *Eng. Fract. Mech.* **158**: 39-58.

30. Wu, Z., H. Rong, J. Zheng and W. Dong (2013) Numerical method for mixed-mode I–II crack propagation in concrete. *J. Eng. Mech.* **139**: 1530-1538.

31. Wang, C., Z. Zhu and H. Liu (2016) On the I–II mixed mode fracture of granite using four-point bend specimen. *Fatigue Fract. Eng. M.* **39**: 1193-1203.

32. Gómez, F., M. Elices, F. Berto and P. Lazzarin (2007) Local strain energy to assess the static failure of U-notches in plates under mixed mode loading. *Int. J. Fracture*. **145**: 29-45.

33. Gómez, F., M. Elices, F. Berto and P. Lazzarin (2009) Fracture of U-notched specimens under mixed mode: experimental results and numerical predictions. *Eng. Fract. Mech.* **76**: 236-249.

34. Berto, F., P. Lazzarin, F. Gómez and M. Elices (2007) Fracture assessment of U-notches under mixed mode loading: two procedures based on the 'equivalent local mode I' concept. *Int. J. Fracture*. **148**: 415-433.

35. Gómez, F., M. Elices, F. Berto and P. Lazzarin (2009) Fracture of V-notched specimens under mixed mode (I+ II) loading in brittle materials. *Int. J. Fracture*. **159**: 121-135.

36. Lazzarin, P., F. Berto, M. Elices and J. Gómez (2009) Brittle failures from U- and V-notches in mode I and mixed I + II mode: a synthesis based on the strain energy density averaged on finite-size volumes. *Fatigue Fract. Eng. M.* **32**: 671-684.

37. Mu, F. and J. Vandenbossche (2016) A superimposed cohesive zone model for investigating the fracture properties of concrete-asphalt interface debonding. *Fatigue Fract.*

Eng. M. doi: 10.1111/ffe.12509.

38. Xu, S. and H. Reinhardt (1999) Determination of double-K criterion for crack propagation in quasi-brittle fracture: Part I Experimental investigation of crack propagation. *Int. J. Fracture*. **98**: 111-149.

39. Xu, S. and H. Reinhardt (1999) Determination of double-K criterion for crack propagation in quasi-brittle fracture: Part II Analytical evaluating and practical measuring methods for three-point bending notched beams. *Int. J. Fracture*. **98**: 151-177.

40. Nagashima, T., Y. Omoto and S. Tani (2003) Stress intensity factor analysis of interface cracks using X-FEM. *Int. J. Numer. Meth. Eng.* **56**: 1151-1173.

41. Dong, W., Z. Wu and X. Zhou (2016) Fracture mechanisms of rock-concrete interface: experimental and numerical. *J. Eng. Mech.* 04016040.

42. RILEM (1985) Determination of the fracture energy of mortar and concrete by means of three-point bend tests on notched beams. *Mater. Struct.* **18**: 285-290.

43. Dong, W., L. Zhang and Z. Wu (2014) Experiment study on tension softening constitutive relation of rock-concrete interface. *J. Hydraul. Eng.* **45**: 712-719.

Appendix I Tables

Table 1: Mechanical properties of rock, concrete and their interface

Material	ρ (kg/m^3)	E (GPa)	ν	f_c (MPa)	f_t (MPa)
Concrete	2400	33.29	0.204	38.96	—
Rock	2668	64.39	0.198	119.2	—
Interface	—	—	—	—	1.371

Table 2: Experimental results of TPB series beams

Specimen	S×D×B (mm×mm×mm)	a_0 (mm)	P_{ini} (kN)	$P_{\max}$ (kN)	K_{1RC}^{ini} (MPa·m$^{1/2}$)	K_{2RC}^{ini} (MPa·m$^{1/2}$)	G_f (N/m)
TPB20-1	400×100×100	20	2.322	2.644	0.332	-0.020	28.256
TPB20-2		22	2.395	2.657	0.373	-0.025	23.373
TPB20-3		22	3.467	3.725	0.539	-0.037	40.342
TPB30-1		30	1.730	2.200	0.335	-0.036	19.300
TPB30-2		31	2.094	2.385	0.412	-0.034	—
TPB30-3		30	1.326	2.068	0.254	-0.021	19.516
TPB40-1		42	1.487	1.746	0.392	-0.036	19.339
TPB40-2		40	1.741	2.162	0.434	-0.039	—
TPB50-1		50	1.154	1.409	0.385	-0.036	25.781
TPB50-2		50	0.755	1.087	0.252	-0.024	21.574
TPB50-3		51	1.075	1.493	0.371	-0.035	31.062
TPB60-1		60	0.577	0.748	0.296	-0.027	11.128

Table 3: Fracture parameters used in the numerical simulations

Specimen	K_{1RC}^{ini} (MPa·m$^{1/2}$)	f_t (MPa)	E (GPa)		ν		G_f (N/m)
			Concrete	Rock	Concrete	Rock	
TPB20-1	0.332	1.371	33.29	64.39	0.204	0.198	28.256
TPB30-1	0.335						19.300
TPB40-1	0.392						19.339
TPB50-1	0.385						25.781
TPB60-1	0.296						11.128
T-, L-, S-series	0.335						19.300

Table 4: Dimensions and numerical results of T series composite beams

Test Series	$S \times D \times B$ (mm×mm×mm)	a_0/D	P_{ini} (kN)	P_{max} (kN)	L_{FPZ}^{max} (mm)
T20		0.2	2.140	2.795	66.0
T30		0.3	1.640	2.160	58.0
T40	400×100×100	0.4	1.250	1.630	52.0
T50		0.5	0.930	1.185	44.0
T60		0.6	0.650	0.795	36.0

Table 5: Dimensions and numerical results of L series composite beams

Specimen	$S \times D \times B$ (mm×mm×mm)	a_0 (mm)	a_0/D	P_{ini} (kN)	P_{max} (kN)	L_{FPZ}^{max} (mm)
L100	400×100×100	30		1.640	2.175	58.0
L150	600×150×100	45		1.980	2.810	84.2
L200	800×200×100	60		2.230	3.325	110.0
L250	1000×250×100	75		2.430	3.755	132.0
L500	2000×500×100	150	0.3	3.380	6.270	232.0
L1000	4000×1000×100	300		5.410	9.575	392.0
L2000	8000×2000×100	600		7.850	14.320	610.0
L5000	20000×5000×100	1500		11.510	24.640	967.5
L10000	40000×10000×100	3000		16.300	36.350	1260.0
L20000	80000×20000×100	6000		20.350	52.750	1520.0

Table 6: Dimensions and numerical results of S series composite beams

Specimen	$S \times D \times B$ (mm×mm×mm)	a_0/D	$D - a_0$ (mm)	P_{ini} (kN)	P_{max} (kN)	L_{FPZ}^{max} (mm)
S1	500×125×100	0.2		2.400	3.240	81.2
S2	576×144×100	0.3		1.950	2.730	82.0
S3	672×168×100	0.4	100	1.550	2.245	82.0
S4	800×200×100	0.5		1.200	1.755	81.2
S5	1000×250×100	0.6		0.800	1.235	81.0

Table 7: Maximum values of K_2/K_1 of L series composite beams

Specimen	Without cohesive force		With cohesive force		Difference of K_2/K_1 with/without cohesive force
	a/D	K_2/K_1	a/D	K_2/K_1	
L100	0.58	0.12032	0.58	0.17526	0.05494
L150	0.55	0.13783	0.55	0.20218	0.06435
L200	0.58	0.15034	0.61	0.22291	0.07257
L250	0.56	0.16026	0.56	0.23929	0.07903

Appendix II Figures

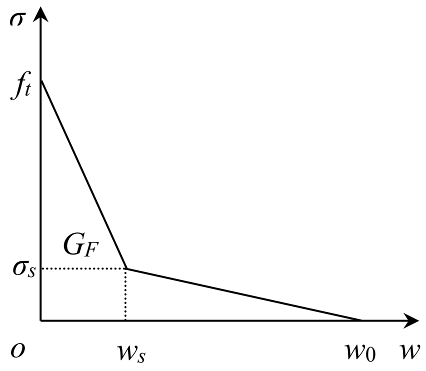

Fig.1. Bilinear stress - crack width curve for softening of rock-concrete interface

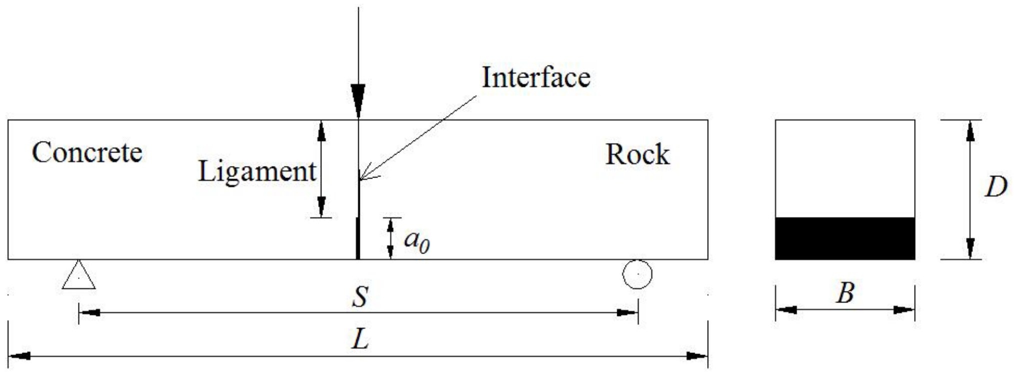

(a) Specimen geometry

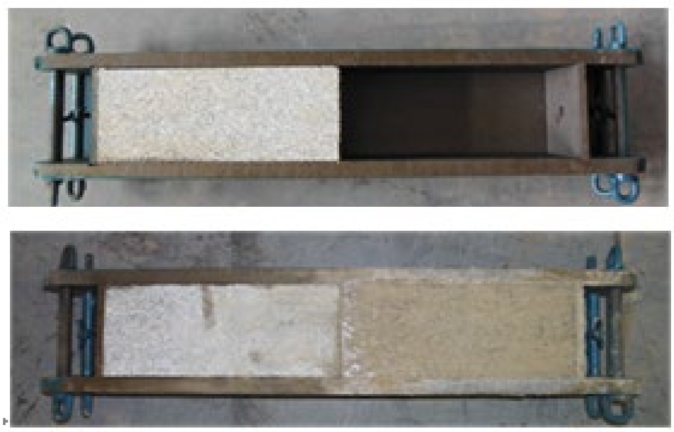

(b) Specimen preparation

Fig. 2. Geometry and preparation of rock-concrete composite specimens

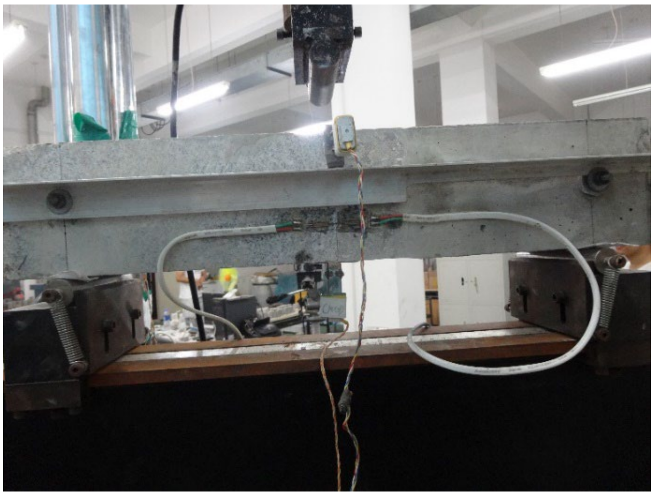

Fig. 3. Three-point bending test setup

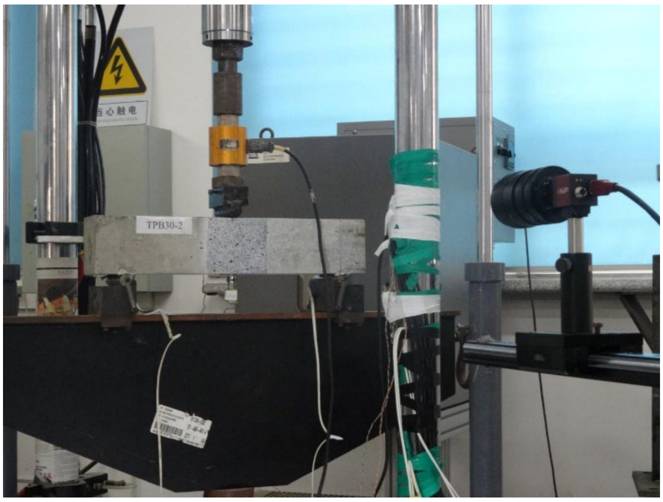

Fig. 4. DIC test setup

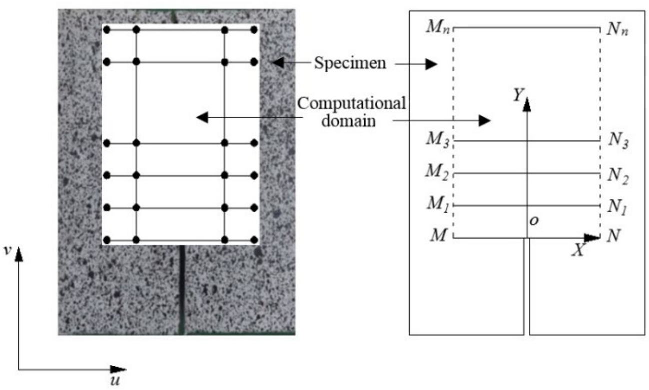

Fig. 5. Computational grids in the DIC test

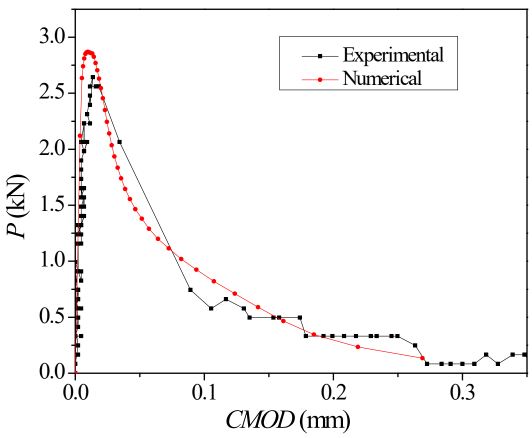

(a) TPB20-1

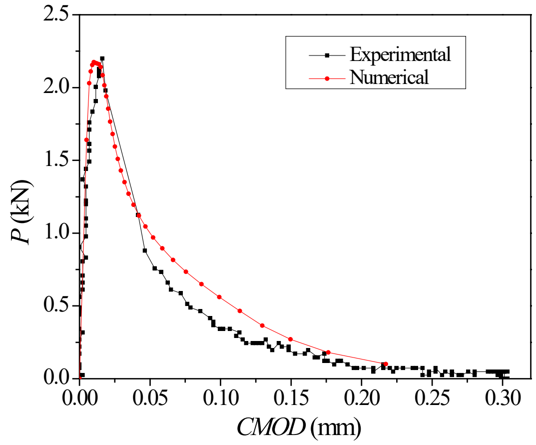

(b) TPB30-1

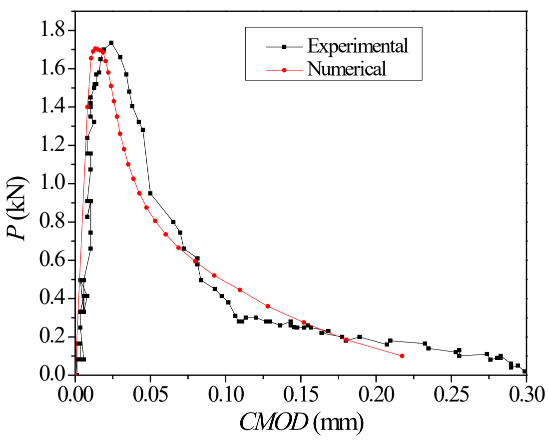

(c) TPB40-1

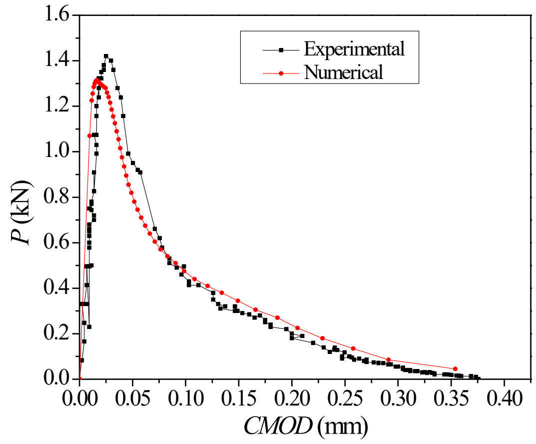

(d) TPB50-1

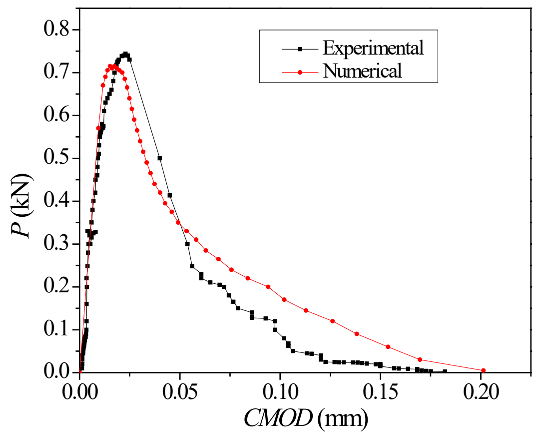

(e) TPB60-1

Fig. 6. Comparison of experimental and numerical P-CMOD curves

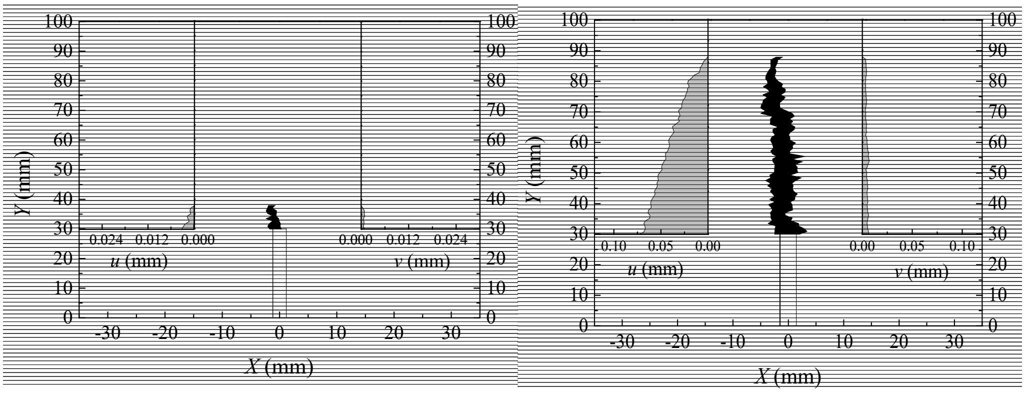

(a) Loading level P_1 (b) Loading level P_2

Fig. 7. FPZ evolution at various loading stages

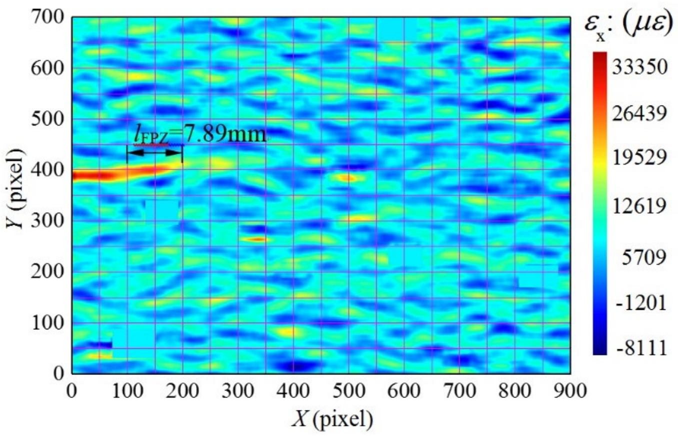

(a) Loading level P_1

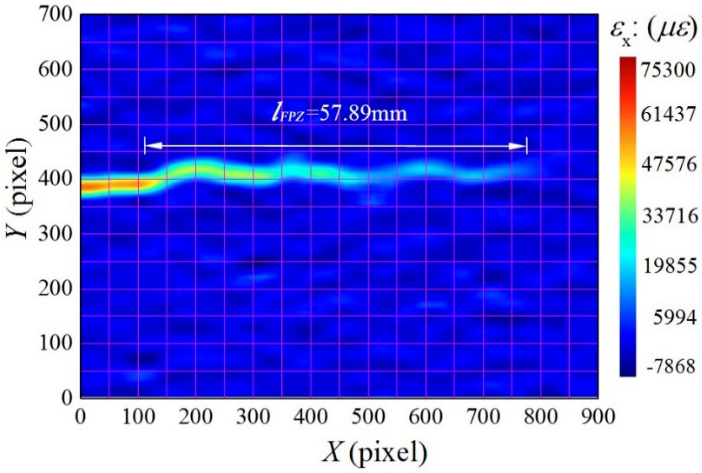

(b) Loading level P_2

Fig. 8. Strain contours at various loading stages

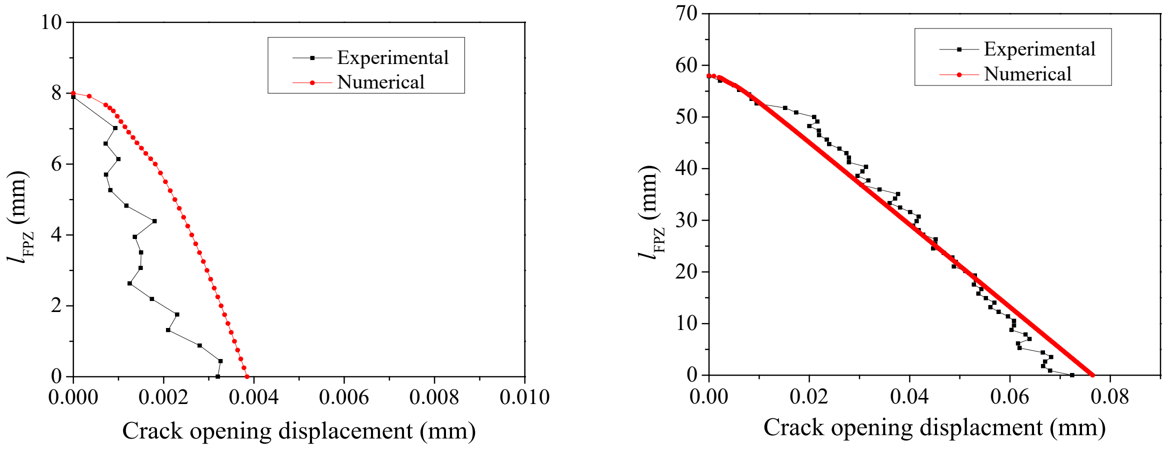

(a) Loading level P_1 (b) Loading level P_2

Fig. 9. Comparison of experimental and numerical crack opening displacement distributions at various loading stages

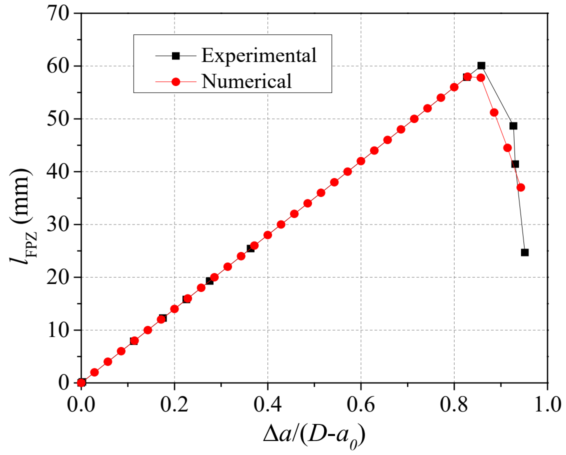

Fig. 10. Comparison of experimental and numerical FPZ evolutions for beam TPB30-1

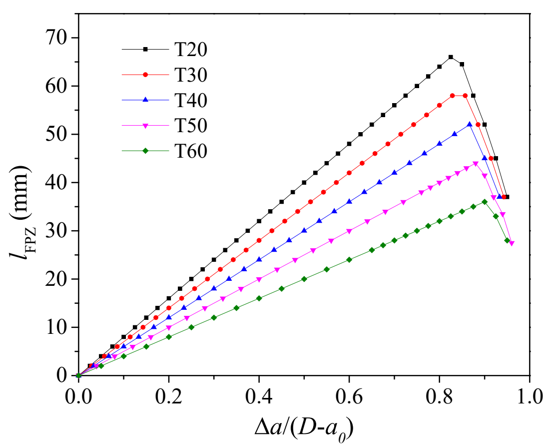

Fig. 11. Variations of FPZ length for T-series beams

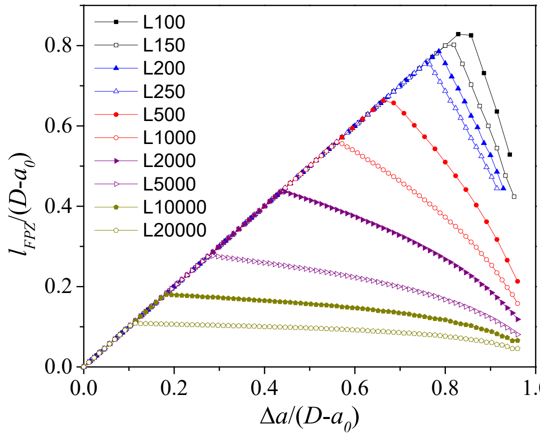

Fig. 12. Variations of FPZ length for L-series beams

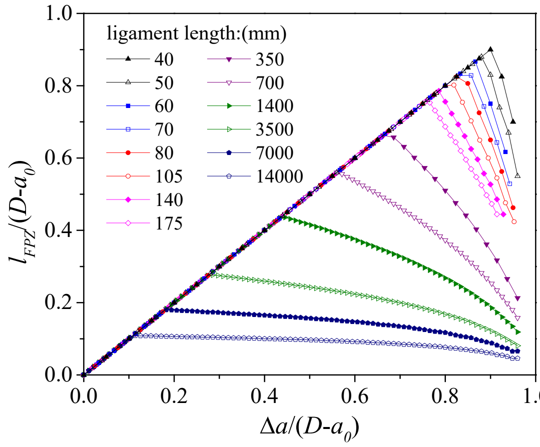

Fig. 13. FPZ evolutions for different ligament lengths

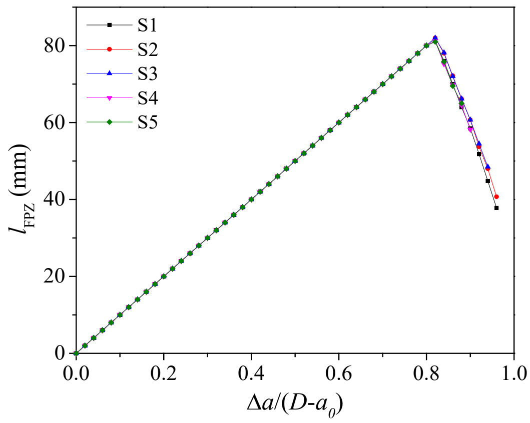

Fig. 14. Variations of fracture process zone for S-series beams

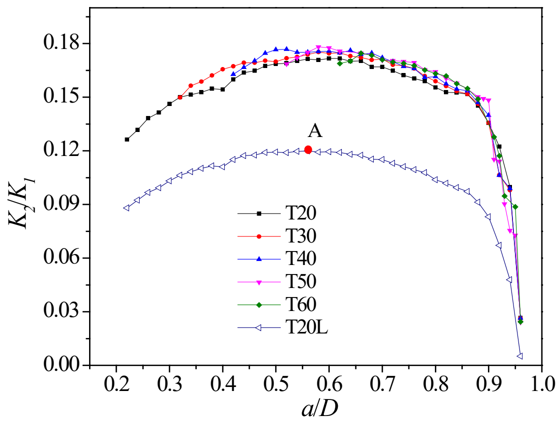

Fig. 15. K_2/K_1 variations during the complete fracture process for T-series beams and T20L

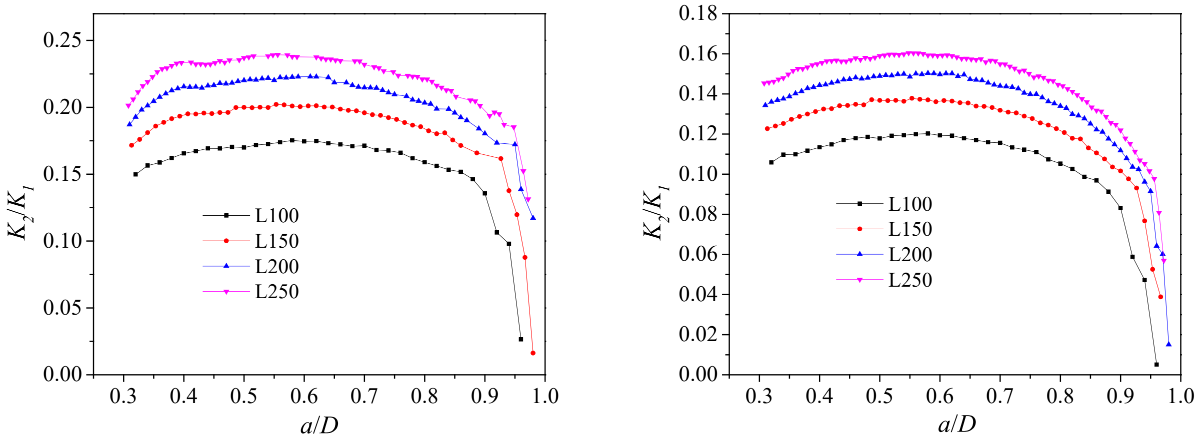

(a) With consideration of cohesive stress (b) Without consideration of cohesive stress

Fig. 16. K_2/K_1 variations during the complete fracture process for L-series beams

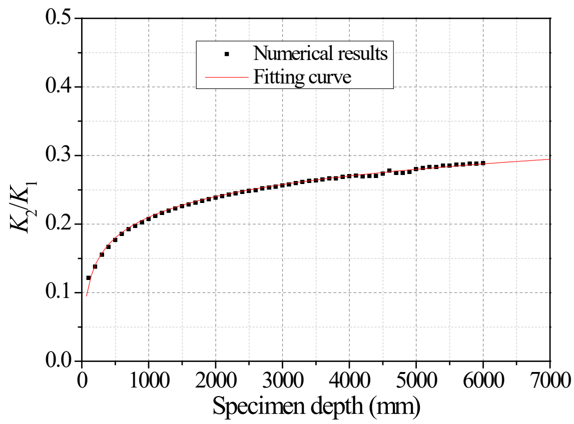

Fig. 17. K_2/K_1 versus beam depth with the fitting curve